How the source depth of coastal upwelling relates to stratification and wind

Jing He[1], **Amala Mahadevan**[2]

[1]MIT/WHOI Joint Program in Oceanography
[2]Woods Hole Oceanographic Institution

Key Points:

- We present a scaling based on balancing wind-driven upwelling and eddy restratification for the source depth in coastal upwelling regions.
- The source depth increases nonlinearly with stronger winds and weaker stratification.
- This has implications for how source depth may change in a more stratified ocean, which affects the upwelling of temperature and nutrients.

Corresponding author: Jing He, jinghe@mit.edu

Corresponding author: Amala Mahadevan, amala@whoi.edu

Abstract

Wind-driven coastal upwelling is an important process that transports nutrients from the deep ocean to the surface, fueling biological productivity. To better understand what affects the upward transport of nutrients (and many other properties such as temperature, salinity, oxygen, and carbon), it is necessary to know the depth of source waters (i.e. "source depth") or the density of source waters ("source density"). Here, we focus on the upwelling driven by offshore Ekman transport and present a scaling relation for the source depth and density by considering a balance between the wind-driven upwelling and eddy-driven restratification processes. The scaling suggests that the source depth varies as $(\tau/N)^{1/2}$, while the source density goes as $(\tau^{1/2}N^{3/2})$. We test these relations using numerical simulations of an idealized coastal upwelling front with varying constant wind forcing and initial vertically-uniform stratification, and we find good agreement between the theory and numerical experiments. This highlights the importance of considering stratification in wind-driven upwelling dynamics, especially when thinking about how nutrient transport and primary production of coastal upwelling regions might change with increased ocean warming and stratification.

Plain Language Summary

Coastal upwelling is a phenomenon where wind blowing parallel to a coast causes water from the deep ocean to be brought up to the surface. Many properties in the ocean–such as temperature, nutrients, oxygen, carbon–exhibit a strong contrast between the surface and the deep ocean, so coastal upwelling is an important process that redistributes these properties in the ocean. For example, nutrient concentration generally increases with depth, and coastal upwelling helps to supply high-nutrient water from the deep ocean to the sunlit surface, which enables the growth of marine plants. Just how much nutrient reaches the surface depends on the strength of upwelling and on the *source depth* from which water is upwelled, which determines its nutrient concentration. We develop and test a theory for predicting the source depth of coastal upwelling based on the strength of the wind and density stratification, i.e. the density contrast between the surface and depth. This theory can help predict how effects of coastal upwelling could be altered in the future from changes in wind and increased stratification due to ocean warming.

1 Introduction

Coastal upwelling driven by alongshore winds is an important physical process that brings water from the deep ocean up to the surface. This upwelling results in the vertical transport and redistribution of oceanic properties and has many consequences. For instance, the upwelling of colder waters from depth can influence regional weather and climate by lowering the sea surface temperature (Izumo et al., 2008). Moreover, the vertical transport of nutrients in coastal upwelling regions fuels high primary production (Chavez & Messié, 2009; Carr, 2001; Messié et al., 2009), and upwelling of dissolved inorganic carbon affects the air-sea exchange of carbon dioxide (Hales et al., 2005; Friederich et al., 2008; Torres et al., 2002).

Coastal upwelling is typically driven by an alongshore wind stress that results in offshore Ekman transport given by $V_E = \tau/\rho f$, where τ is the alongshore wind stress, ρ is the seawater density, and f is the Coriolis parameter. From continuity, the offshore Ekman transport is balanced by upwelling, so V_E is also the volumetric upwelling rate of water per unit length of coastline. Coastal upwelling occurs largely within a Rossby radius of the coast, but farther offshore, Ekman pumping driven by the wind stress curl may also contribute to upwelling (Pickett & Paduan, 2003; Koračin et al., 2004). The vertical velocities arising from the wind stress curl are typically weaker than those associated with offshore Ekman transport, but act over a larger area offshore, and so it may

be important to consider both Ekman transport and Ekman pumping depending on the region of interest (Enriquez & Friehe, 1995; Pickett & Paduan, 2003; Koračin et al., 2004).

Ekman transport theory has been applied extensively to quantify upwelling strength – such as through an upwelling index – based on the magnitude of the alongshore wind stress (e.g. Huyer, 1983; Bakun, 1990; Sydeman et al., 2014). However, Ekman transport, V_E, only describes the volumetric rate of upwelled water, which is just a piece of the puzzle. Because the ocean is stratified with lighter layers of water above denser layers, many properties (e.g. temperature, salinity, nutrients, dissolved inorganic carbon, and oxygen) also exhibit strong vertical gradients in the water column. In a coastal upwelling region, isopycnals tilt up and outcrop near the coast, so the vertical gradients give rise to horizontal surface gradients, which we are then able to observe from satellite imagery. In order to quantify what properties are brought to the surface, it is important to consider the depth from which water originates, i.e. its source depth D_s. For instance, consider a typical temperature distribution that decreases monotonically with depth; upwelling water from 50 m will result in a different SST than if the water upwelled from 150 m. Similarly, instead of depth, we can also think about the density of water that is upwelled, which is useful for properties such as nitrate that correlate strongly with density (Omand & Mahadevan, 2013).

The effect of different upwelling source depths on the SST and phytoplankton productivity are clearly observable in the Arabian Sea (AS) and Bay of Bengal (BoB). Southwesterly winds blow over both basins during the summer monsoon, which causes upwelling along the western coasts of the AS and BoB. Interestingly though, observations show dramatically stronger effects in the AS compared to the BoB. For instance, climatological SST in the western AS cools by 4.4 °C from May to August, while SST in the western BoB only cools by 1.3 °C during this same time frame (Fig. 1). At first glance it might seem that the stronger southwesterly wind stress in the AS (0.19 Nm^{-2} in the western AS compared to 0.06 Nm^{-2} in the western BoB) is chiefly responsible for the different upwelling responses (Fig. 1b). However, the BoB is also strikingly more stratified than the AS year round. The density stratification, characterized by the square of the buoyancy frequency $N^2 = -\frac{g}{\rho}\frac{\partial \rho}{\partial z}$, when depth-averaged over the upper 250 m in the BoB is about double that in the AS (Fig. 1c). Prasanna Kumar et al. (2002) concluded that the weaker wind-driven mixing in the BoB is unable to break through the strong surface stratification and entrain cold nutrient-rich water from below, which explains the higher SST and lower productivity in the BoB compared to the AS. Similarly, stratification would also counter the effect of wind-driven coastal upwelling and contribute to a shallower upwelling source depth near the western margin of the BoB compared to the AS. The contrasting response to coastal upwelling in the AS and BoB motivates the question as to what sets the source depth and source density of upwelling and how these differ between the two basins.

Previous diagnostic methods for estimating source depth include using an offshore density profile and identifying the depth where the density is the same as the onshore surface density (Carr & Kearns, 2003), identifying the intersection of offshore and onshore temperature-salinity diagrams (Carmack & Aagaard, 1977; Messié et al., 2009), and tracking virtual particles in a numerical ocean model (Chhak & Lorenzo, 2007). More recently, Jacox and Edwards (2011, 2012), following the theory of Lentz and Chapman (2004), investigated how the shelf slope and stratification affect the cross-shelf circulation and source depth in a two-dimensional model. They found that the source depth varies with the topographic Burger number, which is dependent on stratification, bottom slope, and f (c.f. Fig. 3 Jacox & Edwards, 2012). However, there was not a direct and generalizable relationship established between the source depth and variables such as the wind stress or stratification. Moreover, the source depth of Jacox and Edwards (2011, 2012) grows monotonically with time, so their results are meant for studying in-

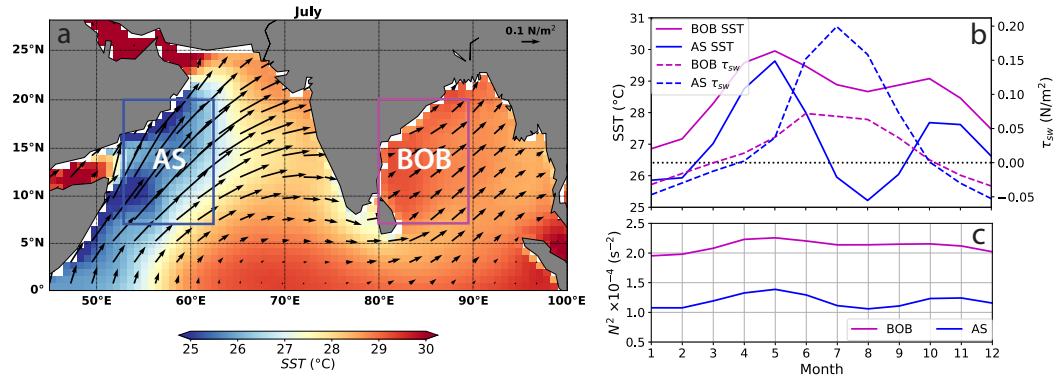

Figure 1. Monthly climatology for the Arabian Sea (AS) and Bay of Bengal (BoB) calculated for the period 1989-2017. **a.** Sea surface temperature (SST, color) and wind stress (arrows) in the Arabian Sea (AS) and Bay of Bengal (BoB) for July. **b.** Seasonal cycle of SST and southwesterly wind stress averaged in the regions denoted by boxes in panel a. **c.** Seasonal cycle of depth-averaged N^2 in the upper 250 m of the ocean in the AS and BoB boxes. SST and wind data are from monthly ERA-Interim Reanalysis (Dee et al., 2011), wind stress is calculated with the Large and Pond (1981) formula, and N^2 is calculated from the MIMOC climatology (Schmidtko et al., 2013) using the Gibbs Seawater Toolbox (McDougall & Barker, 2011).

dividual upwelling events lasting a few days. To predict the source depth on longer timescales, such as over an entire upwelling season, a new theory is needed.

In this study, we move beyond one- and two-dimensional arguments to consider how wind and stratification affect the source depth. Without considering the spatio-temporal variability in the winds or sloping topography that includes a continental shelf and slope, we argue that the source depth in an upwelling region results from a balance between the wind-driven overturning and eddy-driven restratification. It is shown that alongshore winds give rise to an upwelling front that exhibits baroclinic instability (Brink, 2016; Brink & Seo, 2016). These eddies are ubiquitous in upwelling fronts and tend to flatten isopycnals, thereby countering the steepening of isopycnals due to Ekman transport (Durski & Allen, 2005; Capet et al., 2008), and preventing (or slowing) an indefinite increase in the source depth. This countering effect of eddies has been related to reduced nutrient concentrations and primary production in nearshore coastal upwelling regions (e.g. Gruber et al., 2011; Hernández-Carrasco et al., 2014), but to our knowledge, it has not yet been applied to estimating the source depth. We use a three-dimensional numerical model of an upwelling system to experiment with a range of parameters and test the theory. Our theory is applicable in the mean (seasonal or longer-term average) sense to any coastal upwelling region, such as the Eastern Boundary Upwelling Systems (EBUS), and for assessing how such regions may differ from each other or be affected by climate change.

In what follows, we begin, in Sec. 2, by developing a theoretical scaling relation for source depth, D_s as a function of windstress, τ, and stratification, N^2, in a dynamically equilibrated upwelling front. We then extend this to estimate the source density, or the density difference of the source waters from the undisturbed (offshore) surface density. In Sec. 3, we describe the idealized numerical model, experiments, and methods for testing the scaling relation. The results of the numerical experiments and comparison to the scaling relation are presented in Sec. 4. In Sec. 5, we discuss potential implications of the source depth scaling on upwelling regions undergoing climate change before summarizing and concluding in Sec. 6.

2 Theoretical estimate of source depth

To develop a scaling for the quasi-balanced source depth, we begin by considering an idealized ocean initially at rest with horizontal isopycnals and a constant stratification. When a steady upwelling-favorable wind is imposed, an offshore Ekman transport is developed at the surface with a return flow in the interior, which results in an wind-driven overturning circulation denoted by the stream function ψ_w (Fig. 2). As dense water upwells near the coast, isopycnals steepen and outcrop at the surface, creating an upwelling front with a cross-shore buoyancy gradient as described by Allen et al. (1995). If the wind persists in maintaining the upwelling front, the front eventually becomes baroclinically unstable (Durski & Allen, 2005; Brink, 2016) and generates eddies. We assume the diapycnal mixing is small and that most transport occurs along isopycnals, so the effect of the eddies is to adiabatically flatten isopycnals in the along-front mean sense (Lee et al., 1997; Marshall & Radko, 2003). This slumping of isopycnals and re-stratifying of the upper ocean by eddies is described by the eddy stream function ψ_e, which acts in the opposite direction to ψ_w (Fig. 2). A dynamical equilibrium is achieved when the mean along-front wind-driven steepening of isopycnals is countered by the eddy-driven slumping (Fig. 2). This is the same idea as the eddy equilibration mechanism of Marshall and Radko (2003) for the Southern Ocean, except that a coastal upwelling front is on a much smaller scale than the Southern Ocean front (100 km as opposed to 2000 km). Mahadevan et al. (2010) showed that the residual mean framework is also applicable to an open ocean non-quasigeostrophic mixed layer front, and here we follow their approach in balancing ψ_w with ψ_e to solve for the equilibrated source depth.

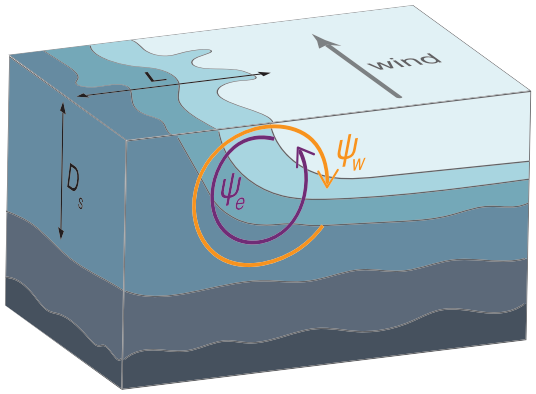

Figure 2. Schematic of a steady state upwelling front in the northern hemisphere. The shading denotes layers of different potential density with isopycnals denoted by the interfacial surfaces. The coast is on the left, and an alongshore wind blowing into the page causes an offshore Ekman transport that results in a wind driven overturning circulation, ψ_w. Baroclinic instabilities produce an opposing eddy-driven circulation (in the along-shore mean) given by the streamfunction ψ_e. The width of the front is L, and the source depth is D_s.

2.1 Source depth scaling

The wind-driven overturning circulation ψ_w is simply given by the Ekman transport

$$\psi_w = \frac{-\tau}{\rho_0 f}, \tag{1}$$

but we need choose a form for the eddy-driven stream function ψ_e. We use the mixed-layer instability parameterization for ψ_e (Fox-Kemper et al., 2008a; Fox-Kemper & Fer-

rari, 2008b), given by

$$\psi_e = C_e \frac{D_s^2 b_y}{f}, \tag{2}$$

where b_y (s^{-2}) is the surface lateral buoyancy gradient, and buoyancy is defined as $b \equiv -g\frac{\rho}{\rho_0}$ (ms^{-2}). The coefficient is $C_e = 0.06$. In the Fox-Kemper et al. (2008a) formulation, the strength of ψ_e depends on the mixed layer depth, but here we use the source depth, D_s, as the vertical scale, since this is the unstratified depth in the upwelling region shoreward of the upwelling front. With this choice for ψ_e, we assume that baroclinic instability is dominant in the upper ocean region of interest, and we later show in Sec. 4 that this choice adequately captures the eddy dynamics in our numerical model. One thing to note is that the baroclinic instabilities represented by ψ_e act in the upper ocean, while the wind-driven overturning circulation acts throughout the water column, so a balance can only be achieved in the upper ocean. However, we are primarily concerned with water entering the mixed layer and reaching the surface, so we focus on the balance of stream functions above the source depth and assume the wind-driven circulation is closed in the interior.

The lateral buoyancy gradient b_y scales as

$$b_y \sim \frac{\Delta b}{L}, \tag{3}$$

where Δb is the surface buoyancy difference across the upwelling front and L is the width of the front (Fig. 2). Typically if a pycnocline is present in the initial conditions, then the upwelled pycnocline is called the upwelling front since it has the greatest density gradient. In the case of 2D upwelling, this upwelling front will move offshore with time due to Ekman transport, so the front width will be narrower and quite different from the distance between the coast and the front (Szoeke & Richman, 1984). However, in our idealized setup with uniform vertical stratification, L extends all the way to the coast and it is proportional to the cross-shore distance over which the isopycnals are sloping, which is the Rossby deformation radius. Though the eddy field will have some affect the surface front width, we take L to be the proportional to the Rossby radius of deformation. Lentz and Chapman (2004) found $L = 4ND_s/f$ from simulations of multiple coastal upwelling regions, and we also find that taking $L = 4ND_s/f$ generally agrees with the surface expression of the front across our simulations (see Fig. S3; Supplementary materials).

Next, the stratification N^2 is defined as the vertical buoyancy gradient b_z, which is approximately

$$N^2 = b_z \sim \frac{\Delta b}{D_s}, \tag{4}$$

where Δb is now the buoyancy difference between the surface and at a depth D_s. If we assume that coastal upwelling simply tilts isopycnals so that vertical buoyancy gradients become lateral surface buoyancy gradients, then Δb in Eqs. (3) and (4) are the same. This allows us to substitute $\Delta b = N^2 D_s$ from Eq. (4) into Eq. (3), and we can now relate the lateral buoyancy gradient to stratification and the source depth. Further, substituting $L = 4ND_s/f$ into Eq. (4) yields $b_y = Nf/4$.

Lastly, balancing ψ_w with ψ_e from Eqs. (1) and (2) and making the substitution $b_y = Nf/4$ yields the following scaling estimate for the source depth

$$D_s = C_s \left(\frac{\tau}{\rho_0 N f} \right)^{1/2}, \tag{5}$$

where $C_s = (4/C_e)^{1/2} = 8.16$ for $C_e = 0.06$. Equation (5) tells us that $D_s \sim \tau^{1/2}$, as stronger winds drive greater offshore Ekman transport, resulting in the upwelling of deeper water. Conversely, $D_s \sim N^{-1/2}$, since increased stratification creates a larger lateral

density gradient, which strengthens the eddy overturning circulation (Eq. 10) to reduce upwelling depth. Lastly, the 1/2 power-law in Eq. (5) implies that source depth is most sensitive to changes when τ/N is small, i.e. in strongly stratified regions with weak wind.

Interestingly Eq. (5) gives the same scaling as the Pollard-Rhines-Thompson (PRT) wind-driven mixed layer depth as both are dependent on $(\tau/\rho_0 f N)^{1/2}$. However, Eq. (5) arises from a different process (balancing eddy restratification with upwelling) than the Richardson-number criteria that is used for the PRT depth (Pollard et al., 1973). One difference is that the coefficient for the PRT depth is around 0.57-1.29 (Lentz, 1992), while the coefficient in Eq. (5) is about 8 times larger. It makes sense that the source depth varies in a way similar to the mixed layer depth since the source depth has to be at least as deep as the mixed layer depth. Moreover, it is reassuring that the PRT depth has been shown to match well with observed mixed layer depths in upwelling regions around the world (Lentz, 1992; Dever et al., 2006), and the onshore velocities are found to peak below the PRT depth (Dever et al., 2006). So it seems reasonable that the source depth would correlate with the PRT depth, but be deeper overall.

2.2 Density of upwelled water

While it is intuitive to think of a source depth, many variables of interest in the ocean–such as temperature and nitrate–have a stronger correlation with density than depth (Omand & Mahadevan, 2013). Thus, depending on the application, it may be useful to think in terms of the density of upwelled water instead of its source depth. We denote the upwelling density as a density offset $\Delta\rho$ from offshore surface waters ρ_{offshore}, so the true density of water upwelled near the coast is equal to $\Delta\rho + \rho_{\text{offshore}}$.

To obtain a scaling relation for $\Delta\rho$, we use Eq. (4) to make the substitution $D_s = -\frac{g}{\rho_0}\frac{\Delta\rho}{N^2}$ in Eq. (5). Equation (5) can then be recast as a scaling relationship for $\Delta\rho$ as a function of the wind stress and stratification:

$$\Delta\rho = \frac{C_s}{g}\left(\frac{\rho_0\tau}{f}\right)^{1/2} N^{3/2}. \tag{6}$$

In contrast to the source depth in Eq. (5), the density offset scales with $N^{3/2}$ since larger vertical density gradients (N^2) result in a greater surface lateral density difference ($\Delta\rho$) and equivalently, a larger density offset from the source of upwelling. $\Delta\rho$ scales as $N^{3/2}$ instead of N^2, because stronger stratification also strengthens the eddy overturning circulation and weakens upwelling. Thus, eddies reduce the extent to which stratification influences the density offset, but $\Delta\rho$ still has a stronger dependence on stratification than wind. Any combination of wind stress and stratification yields a unique source depth and density offset, which means we can use D_s and $\Delta\rho$ interchangeably and easily convert between the two.

3 Methods

To evaluate Eqs. (5) and (6), we use a three-dimensionsal (3D) numerical ocean model configured in a periodic channel with stratification and wind stress that represent the range observed in the Arabian Sea and Bay of Bengal. We run simulations with different values of wind stress and initial stratification to test how the source depth and density offset respond. In these simulations, we use a constant value of wind stress and uniform N^2 for the majority of cases, although we also test the scaling with more realistic profiles of $N^2(z)$. From the model outputs, we calculate the source depth D_s and density offset $\Delta\rho$ based on the upwelling in the 3D numerical model and compare those to theoretical estimates of D_s and $\Delta\rho$ from Eqs. (5) and (6).

3.1 Numerical model

We use the Process Study Ocean Model, which numerically solves the nonhydrostatic Bousinesq equations (Mahadevan et al., 1996a, 1996b). The model domain is a flat-bottomed re-entrant channel on an f-plane centered at a latitude of 15°N, approximately the mid-latitude of the AS and BoB. The channel extends 96 km in the alongshore (x) direction, 384 km in the cross-shore (y) direction, and has a total depth of 500 m (in the z direction). The horizontal grid resolution is 1 km, and there are 32 stretched vertical levels ranging in thickness from 1 m at the surface to 36 m at the bottom. A horizontal resolution of 2 km is also tested and it did not significantly alter the source depth, but we use 1 km which is consistent with Durski and Allen (2005). The boundary conditions are periodic in the alongshore direction, and no-flow boundary conditions are enforced at the walls in the cross-shore direction. The cross-shore width is chosen to be large enough so that the offshore boundary does not influence the upwelling dynamics at the coast located at $y = 0$ km. Deepening the domain to 1000 m and doubling the width of the channel in the y direction has no significant effect on the source depth. The model is initialized with the same vertical density profile throughout the domain and is started from a state of rest with no initial horizontal gradients.

A wind stress $\tau = (\tau^x, 0)$ is applied in the negative x direction, which drives upwelling at the coast located at $y = 0$ (Fig. 3). The alongshore wind stress is $\tau^x = -\tau_{max}$ everywhere except near the offshore wall, where τ^x decays linearly to 0 from $y = 234$ km to $y = 385$ km to spread the downwelling over a large area far offshore. At the start of the model run τ is increased linearly from 0 to τ^x over the first 10 days to gradually spin up the model and avoid generating strong internal waves. After day 10, the wind stress is held constant.

To test the validity of explaining source depth with the dynamical equilibrium proposed, we need to be careful with the model mixing scheme. Here, we aim to characterize the source depth that results from the balance between coastal upwelling and eddy-restratification, which are both largely adiabatic processes. But, the source depth could also deepen due to vertical mixing, a diapycnal process. In order to focus on the adiabatic processes, we use a simple mixing scheme that results in a predictable mixed layer depth, which is less than the source depth. This ensures that the source depth is not influenced by diabatic mixing. In the horizontal, we use a constant eddy diffusivity and viscosity of $K_h = 1$ m^{2}s^{-1} in all the simulations. The vertical eddy diffusivity and viscosity K_z is dependent on the wind stress and is parameterized following Mahadevan et al. (2010) as

$$K_z = \max\left\{\frac{1}{2}K_{max}\left[1 + \tanh\left(\frac{z+\delta_E}{\Delta}\pi\right)\right], K_{min}\right\}, \tag{7}$$

where $\delta_E = \frac{0.4}{f}\left(\frac{\tau}{\rho}\right)^{1/2}$ is the depth of the surface Ekman layer and Δ (m) is the transition height (see Fig. 3). All of the numerical experiments used $K_{max} = 10^{-2}$ m^{2}s^{-1}, $K_{min} = 10^{-5}$ m^{2}s^{-1}, and $\Delta = 0.5\delta_E$, based on Mahadevan et al. (2010).

Equation (7) creates a surface mixed layer whose thickness depends on the wind stress while neglecting the effect of air-sea buoyancy fluxes (e.g. heating or cooling), which are not included in the model. A constraint is that the source depth D_s cannot be shallower than the mixed layer depth MLD, and is in fact much deeper in the simulations. By purposefully making the model mixing independent of N^2, we are able to evaluate the effect of N^2 on the eddy restratification process without concern that lowered stratification might increase mixing, and thereby enhance the source depth. If we were to use a more sophisticated, but less interpretable, turbulence closure scheme –such as Mellor-Yamada , k-ϵ, or K-Profile Parameterization (Wijesekera et al., 2003; Mukherjee et al., 2016)– as is commonly used in coastal settings, then it would less clear how much vertical mixing affects the source depth. This would make it more difficult to isolate the dependence of source depth on the balance between ψ_w and ψ_e.

We run nine experiments varying the initial N^2 between 10^{-5} and 10^{-4} s^{-2} and varying τ_{max} between 10^{-2} and 10^{-1} Nm^{-2}. These values were chosen to approximately span the range of observed wind stress and N^2 (averaged over the top 500 m) in the Arabian Sea and Bay of Bengal. While the southwesterly wind stress reaches 0.2 Nm^{-2} in the Arabian Sea, this high a value was difficult to implement, since the wind in the model blows constantly for months and it would necessitate a very small time step. So we cap the highest constant wind stress in our model simulations at 0.1 Nm^{-2}. Three additional experiments are run with the initial $N^2(z)$ varying with depth to test the effects of using more realistic density stratification profiles. For these three experiments, we vary the thickness of the initial mixed layer (ML) and the peak stratification in the initial profile N^2_{peak}, but maintain the same depth-averaged stratification in the upper 250 m. These additional three experiments are further explained in Sec. 4.3. Table 3.1 summarizes the parameters used in each experiment. Each simulation is integrated forward in time with a time step of 108 s (for $\tau_{max} = 0.1$ Nm^{-2}) or 216 s (all other experiments) for at least 30 days after the upwelling front becomes unstable. The total time period of the simulations ranged from 60 days to 180 days, depending on how long it takes for the front to become unstable. Outputs are saved at 1-day intervals.

Our simulations are designed to be as simple as possible while still capturing the dynamics of interest - i.e., the competition between the wind-driven upwelling and eddies. As a result, several other factors that could affect upwelling are neglected. To start, we ignore bottom topography, which introduces different dynamics and has been shown to affect the source depth by upwelling deep water along the bottom boundary layer (Lentz & Chapman, 2004; Jacox & Edwards, 2011, 2012). Here we focus on upwelling just from the interior and not coming up slope through the bottom boundary layer. Moreover, Brink (2016) found that the available potential energy for baroclinic instability, as well as the eddy kinetic energy and eddy length scale, all depend on the bottom slope. In addition, there is no bottom friction in the experiments shown here; we find that the inclusion of bottom friction does not significantly alter the source depth, so it is omitted to exclude having another parameter to tune. Because a constant wind stress is applied for months in the model, we see unrealistically large horizontal velocities of up to 2 ms^{-1} in some simulations. For simplicity though, we keep the wind stress constant in time, without any cross-shore component, or any significant wind stress curl. Lastly, a consequence of the minimal mixing is that surface Ekman transport sometimes results in unstable density profiles near the surface. This could be remedied by adding a convective mixing scheme, but is avoided because we find it results in unrealistic horizontal grid-scale gradients (Cessi, 1996). We think that these unrealistic artifacts of the model do not affect the overall results of this study.

3.2 Source depth calculation

We determine the "true" source depth in the model by using passive tracers to track the initial depth of water parcels. The model is initialized with 32 separate passive tracers, one at each vertical level. Each tracer is initialized to have a concentration of 1 in its starting grid cell and 0 everywhere else. As water advects in the model, each grid cell will have a combination of tracers from various starting depths. We obtain a single source depth for each grid cell by taking a weighted average of all the initial depths of the tracers present, weighted by the tracer concentrations. Mathematically, this is defined as

$$D_s = \frac{\sum_{i=1}^{M} c_i d_i}{\sum_{i=1}^{M} c_i}, \tag{8}$$

where M is the number of tracers (32 in this case), d_i is the initial depth of tracer i, and c_i is the concentration of tracer i. The density offset $\Delta\rho$ is related to the source depth D_s through the definition of stratification $N^2 = -\frac{g}{\rho_0}\frac{\Delta\rho}{D_s}$. Thus, we convert from D_s calculated in the model to $\Delta\rho$ using $\Delta\rho = -\frac{\rho_0}{g}N^2 D_s$, where the initial constant stratification is the value used for N^2.

Table 1. Alongshore wind stress τ_{max}, depth-averaged initial stratification (N^2_{avg}) in upper 250 m, and details about the shape of the initial N^2 profile for the various simulations in this paper. The first nine experiments are initialized with an uniform N^2 profile. The experiments "small peak," "large peak," and "deep ML" are initialized with non-constant N^2 profiles with varying mixed layer thickness (ML) and peak N^2 values (N^2_{peak}) (Fig. 9).

Experiment	τ_{max} ($\mathrm{Nm^{-2}}$)	N^2_{avg} ($\mathrm{s^{-2}}$)	N^2 shape	
lowW_lowN	10^{-2}	10^{-5}	constant	
lowW_medN	10^{-2}	5.5×10^{-5}	constant	
lowW_highN	10^{-2}	10^{-4}	constant	
medW_lowN	$5.5\times\ 10^{-2}$	10^{-5}	constant	
medW_medN	$5.5\times\ 10^{-2}$	5.5×10^{-5}	constant	
medW_highN	$5.5\times\ 10^{-2}$	10^{-4}	constant	
highW_lowN	10^{-1}	10^{-5}	constant	
highW_medN	10^{-1}	5.5×10^{-5}	constant	
highW_highN	10^{-1}	10^{-4}	constant	
			ML (m)	N^2_{peak} ($\mathrm{s^{-2}}$)
small peak*	10^{-1}	10^{-4}	25	10^{-3}
large peak*	10^{-1}	10^{-4}	25	2×10^{-3}
deep ML*	10^{-1}	10^{-4}	75	10^{-3}

*See Sec. 4.3 for more details.

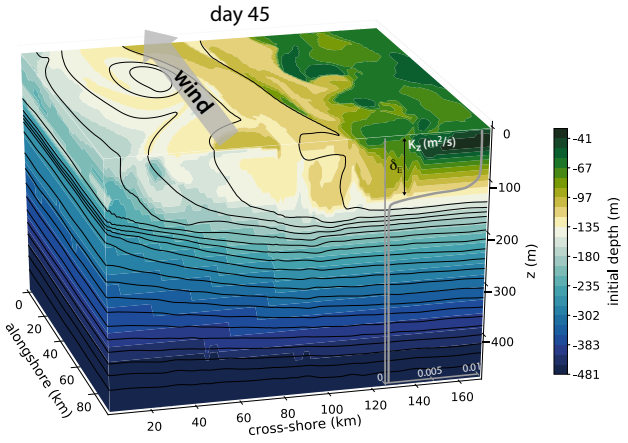

Figure 3. Model setup and snapshot of isopycnals (black contours, interval of 0.15 $\mathrm{kg/m^3}$) and depth tracers at day 45 for experiment highW_highN (Table 3.1). A steady alongshore wind blows into the page, driving coastal upwelling at the western coast of the domain. The initial depth of the dominant tracer in each grid cell is shown in colors, and the shape of the vertical diffusivity (and viscosity) K_z profile is also indicated.

We calculate the source depth over a time period when the model has achieved a dynamic equilibrium. This is identified as a 20 day period of the model run with the minimal change in eddy kinetic energy (EKE) (Supporting Information, Fig. S1,S2). The EKE is calculated as $EKE = \frac{1}{2}(u'^2 + v'^2 + w'^2)$, where u', v', w' are respectively the alongshore, cross-shore, and vertical velocity anomalies from the alongshore mean. For

each simulation, we identify the period of dynamic equilibrium as the 20-day period where the linear regression of the depth-averaged EKE in a nearshore 150 km band has the smallest slope, so the change in EKE with time is minimal during this period. We also find that our main results are robust to different choices of the 20-day time windows.

Then for each day, we determine the source depth for a particular simulation by averaging over the upwelling area, defined by a distance r from the coast and a depth δ from the surface. We take r to be 30 km to represent a narrow coastal band where the deepest isopycnals are outcropping right at the coast. As for δ, since we are considering water parcels that reach the surface, we choose δ to include just the top 3 layers of grid cells representing the upper 11.7 m. We find that varying δ between the top 2 to 4 grid cells (which changes δ between 6.1 and 17.6 m) and varying r between 10 and 40 km alters the source depth by about 10 m. Averaging over the area given by r and δ gives a single source depth for each cross-shore transect in the model. The source depth is then calculated according to Eq. (8) for each day of the 20-day period and for each cross-sectional slice in the alongshore direction (we average 96 cross-shore slices of the model over 20 snapshots, i.e., over $n = 1920$ realizations). We report the median D_s during this period, as well as the 10th and 90th percentile values.

4 Results

4.1 Evolution of model eddy field

We now have everything we need to estimate D_s and $\Delta\rho$ from the scaling relations developed in Sec. 2 (Eqs. 5 and 6) and compare those to the actual source depths and density offsets calculated from tracers. But before doing that, we first show that the model produces reasonable upwelling dynamics and check that our assumption of a dynamic equilibrium is valid. Prior the onset of instabilities, the model produces the expected two-dimensional Ekman response (Fig. 4a). There is an offshore Ekman transport in the surface boundary layer with a weak return flow distributed throughout the interior, which is consistent with previous descriptions of coastal upwelling (e.g. Allen et al., 1995; Brink, 1983; Huyer, 1983; Lentz & Chapman, 2004). Isopycnals steepen and outcrop near the coast, and we see the formation of a lateral density front and an alongshore surface-intensified jet in the same direction as the wind (Fig. 4a). Note that the jet velocities are larger than what is observed in the ocean because the wind is blowing nonstop in our model over many days, and the example shown is a strong wind case. Moreover, the upwelling transport in the model, calculated from integrating vertical velocities within a Rossby radius of the coast at the Ekman depth, is consistent with the theoretical value given by $\tau/\rho f$.

Far offshore, beyond the region of interest, isopycnals are flat and the flow is barotropic, so the onshore return flow is uniformly distributed with depth below the mixed layer. One concern, with two-dimensional models or channel models such as ours, is that if the model is run for long enough, the deep offshore waters will reach the coast and the model will no longer be realistic. However, our simulations are not run long enough that this is an issue. For example, on day 20 in experiment highW_highN shown in Fig. 4a, the onshore return flow is approximately barotropic around 275 km offshore with a velocity < 0.01 ms^{-1}. It would take over 300 days for water from $y = 275$ km to reach the coast, which is far longer than the length of any of our simulations (which extend up to 180 days at most). Furthermore, 300 days is a lower-bound estimate and this timescale will be much larger for simulations with a weaker wind and weaker cross-shore velocities.

As the wind forcing persists, the front continues to intensify until it becomes baroclinically unstable (Fig. 4b). The emergence of eddies can be seen in the surface fields as well as in the EKE (Fig. S1), which is initially zero during the spin-up of the simulations and then sharply increases when instabilities emerge. The onset of instabilities

takes anywhere from 30 days for the high wind stress simulations, to over 100 days for the lower wind stress simulations. As expected, the EKE increases with stratification (due to an increased source of available potential energy) and wind stress. The EKE is typically much larger than the mean kinetic energy (Fig. S1). This behavior is consistent with the findings of Brink (2016). Lastly, there is a range of front widths L across the various simulations, which can be seen qualitatively in Fig. 6. Overall the front widths are consistent with the Rossby deformation radius. For a given stratification, medium and high winds result in a wider front since D_s is greater. And for a fixed wind stress, medium and high stratification gives rise to larger L than weak stratification.

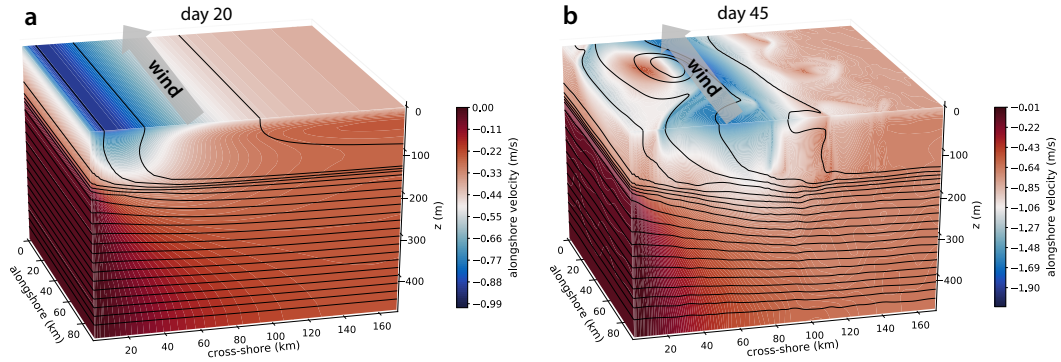

Figure 4. Alongshore velocity u (colors) and density (black contours) at days 20 and 45 of experiment highW_highN (Table 3.1). **a.** Initially, after the alongshore wind is turned on, there is a 2D response that produces an upwelling front and an alongshore geostrophic jet. Deeper isopycnals outcrop near the coast and are nearly vertical in the upwelling region. **b.** At a later time, the front then becomes baroclinically unstable and the resulting eddies slump the isopycnals. The density contour interval is 0.15 kg/m^3. This is an idealized model setup with a constant wind blowing continuously, so the lateral velocities are larger than what would be observed in the real ocean.

Next, we check the plausibility of assuming a balance between ψ_w (Eq. 1) and ψ_e (Eq. 2). Qualitatively, we see from Fig. 4 that eddies re-stratify the surface; the isopycnals are less vertical on day 45, a few days after the onset of baroclinic instabilities, as compared to day 20. We also directly calculate and compare ψ_w (Eq. 1) and ψ_e (Eq. 2) from the model fields (Fig. 5) to evaluate the balance between the wind-driven steepening and eddy-driven slumping of isopycnals. Similar to Mahadevan et al. (2010), we calculate ψ_w from the model velocity fields as

$$\psi_w = -\int_0^z \bar{v}\, dz = \int_0^y \bar{w}\, dy, \tag{9}$$

where the overbar denotes an alongshore average. The eddy stream function ψ_e is typically defined as $\psi_e = \overline{v'b'}/\bar{b}_z$ in the interior (Andrews & McIntyre, 1976) and $\psi_e = \overline{-w'b'}/\bar{b}_y$ for the boundary layer (Held & Schneider, 1999). These two forms were combined into a more general definition in Cerovečki et al. (2009), in which a coordinate stretching factor ϵ is added to correct for the small aspect ratio seen in the ocean and in our model. Here, we use the Cerovecki formulation of ψ_e that is also used in Mahadevan et al. (2010):

$$\psi_e = \epsilon \left(\frac{\epsilon \overline{v'b'}\bar{b}_z - \frac{1}{\epsilon}\overline{w'b'}\bar{b}_y}{\bar{b}_y^{\,2} + \epsilon^2 \bar{b}_z^{\,2}} \right), \tag{10}$$

where the primes denote deviations from the alongshore mean ($v' = v - \bar{v}$, $w' = w - \bar{w}$), and $\epsilon = 10^{-3}$ is a dimensionless vertical stretching factor. Mahadevan et al. (2010) found that the results are not sensitive to varying ϵ between 10^{-2} and 10^{-4}.

A cross-sectional slice of ψ_w and ψ_e calculated using Eqs. 9 and 10 on day 45 for experiment highW_high_N (Table 3.1) is shown in Fig. 5. The colorbars are scaled so that positive values are orange and negative values are purple, with white being zero. As expected, ψ_w is predominantly positive, indicating a clockwise circulation that upwells dense water near the coast at $y = 0$ (Fig. 5a). On the other hand, ψ_e is mostly negative, so it drives a counter-clockwise circulation that opposes ψ_w (Fig. 5b). Averaged over the region of sloping isopycnals (130 km from the coast), ψ_e and ψ_w are similar in magnitude and approximately balance each other above the source depth (Fig. 5c). The Fox-Kemper et al. (2008a) parameterization for mixed-layer instabilities ψ_{MLI} is shown in the gray-dashed line in Fig. 5c, and it seems to be an appropriate choice since it adequately captures the eddy activity in the simulations. We also experiment with using the paramterization of Marshall and Radko (2003) for mesoscale eddies, but it does a much poorer job of capturing the vertical structure and magnitude of ψ_e in our model. Thus, we feel confident in our choice of eddy parameterization and assumption of a quasi-balanced state in the overturning.

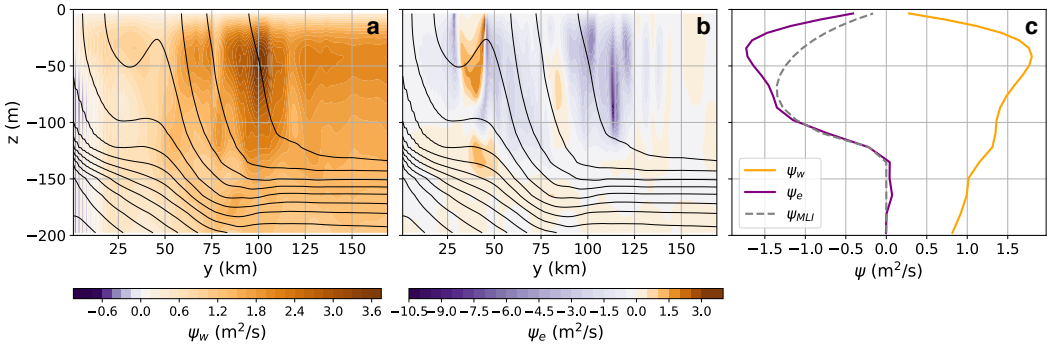

Figure 5. **a.** Wind-driven overturning stream function ψ_w and **b.** eddy-induced overturning stream function ψ_e for experiment highW_highN (Table 3.1). The cross section is located at x=48 km on day 45. The colorbars are scaled so that zero is white, positive values are orange, and negative values are purple. **c.** Stream functions averaged over the region of sloping isopycnals (from the coast to y=130 km) in the cross-shore direction. The Fox-Kemper et al. (2008a) parameterization for mixed-layer instabilities ψ_{MLI} is also shown in the dashed gray line.

4.2 Evaluation of scaling relations

Finally, we can use our model experiments to assess the scaling relations for source depth (Eq. (5)) and density offset (Eq. (6)). Figure 6 shows a snapshot of the source depth calculated from tracers across the nine main simulations (Tab. 3.1). In general, for a given stratification, the source depth increases as expected with stronger winds. For a fixed wind stress, we see the source depth decreasing with higher stratification as predicted by Eq. (5). In addition, the density contours in Fig. 6 are all at the same 0.05 kgm^{-3} intervals, which allows us to compare the density offset ($\Delta\rho$, i.e. the difference in density across the front) between simulations. It is clear that $\Delta\rho$ is directly related to stratification, as evidenced by the increasing number of contours as stratification increases, which is consistent with Eq. (6). One point to highlight is that a deeper source depth does not necessarily imply a larger density offset, which is what we might intuitively expect. This is because the conversion from D_s to $\Delta\rho$ depends on N^2, so the stratifica-

tion plays an important role in determining $\Delta\rho$. An example of this can be seen in Figs. 6c and 6i. The former simulation has a much deeper D_s of over 250 m and a $\Delta\rho$ of about 0.15 kgm^{-3} (Fig. 6c), while the latter case has a shallower D_s of about 140 m and a much larger $\Delta\rho$ of approximately 0.8 kgm^{-3} (Fig. 6i).

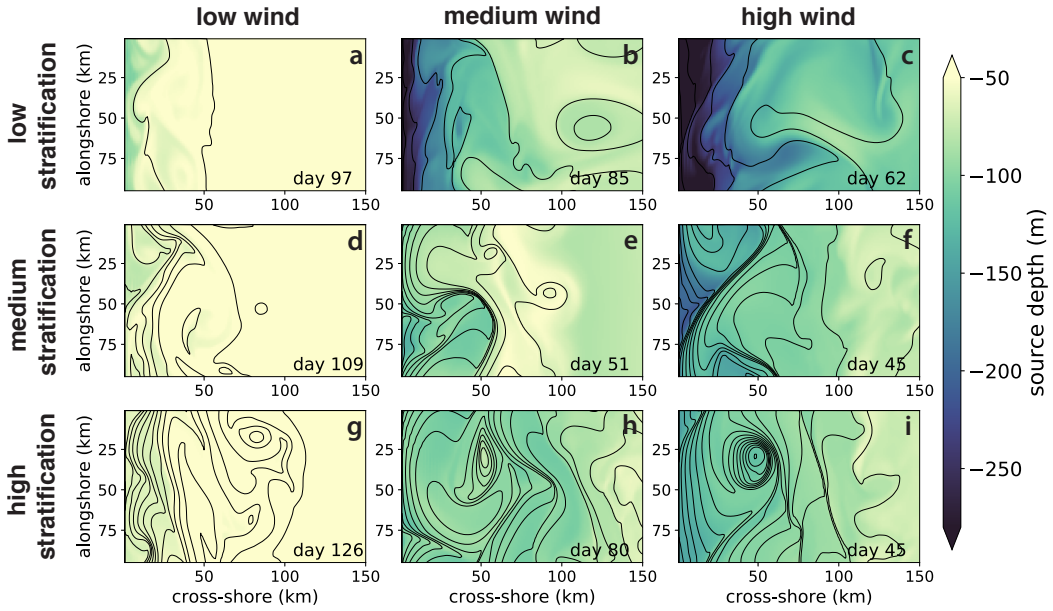

Figure 6. Surface isopycnals (black contours) and source depth (color) in each grid point for a snapshot in time in each of the nine main simulations with constant stratification (Tab. 3.1). The source depth is calculated from tracers and averaged in the top 3 grid cells representing the upper 11.7 m of the ocean, and the day from which the snapshot is taken is midpoint of the 20-day analysis period for each simulation. The isopycnal interval is 0.05 kgm^{-3}.

To more quantitatively assess the agreement between the "true" tracer-estimated source depth and Eq. (5), we compare the range of D_s calculated from the model against the theoretical predictions. Figure 7 is a scatter plot showing the median source depth from tracers with error bars denoting the 10th and 90th percentiles. The 1:1 linear regression line representing perfect agreement between Eq. (5) and the tracer-calculated D_s is shown and it has a correlation coefficient of $r^2 = 0.93$. The r^2 value is calculated for the nine experiments that are initialized with a constant N^2 (Table 3.1), which are the black points in Fig. 7. Not only is there good correlation between the modeled and predicted D_s–which gives us confidence in the 1/2 power law relation–but Eq. (5) also captures the right magnitude of the source depth. The mean and standard deviation of the absolute error is 11.88 ± 8.84 m. The source depth in our simulations range from 50–280 m, so an average error of about ten meters makes Eq. (5) sufficient for order-of-magnitude estimates.

There are two outliers on the lower left of Fig. 7 with $D_s \sim 60$ m that are higher than predicted and do not fall on the 1:1 line very well. These points correspond to the lowW_medN and lowW_highN simulations (Table 3.1), which have predicted source depths of 48 m and 42 m, respectively, according to Eq. (5). The predicted source depths for these two experiments turn out to be very close to the Ekman depth δ_E from Eq. (7), whose value is $\delta_E = 33$ m with a transition depth of $\Delta = 16.5$ m. Thus, these two experiments may be examples in which the turbulent surface mixed layer given by Eq. 7

is actually too deep, and as a result, the source depth in the model is deepened due to mixing.

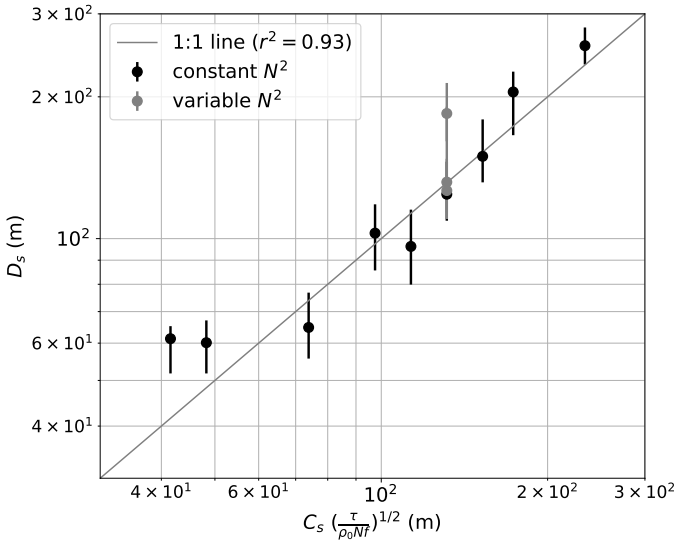

Figure 7. "True" source depth calculated from tracers in the numerical model (D_s) compared to the scaling relation in Eq. (5) $C_s(\frac{\tau}{\rho_0 N f})^{1/2}$. The median value is shown with error bars denoting the 10th and 90th percentiles, and the gray line shows the 1:1 line. ρ_0 is taken to be constant reference density of 1027 kg/m^3.

For completeness we can conduct the same comparisons between the true density offset in the model and predictions of Eq. (6), which is shown in Fig. 8. Similar to Fig. 7, the points closely follow the 1:1 line and the correlation coefficient is very high with $r^2 = 0.95$. Again, the r^2 value is calculated only for the black points which are the experiments with a constant initial N^2. We should not expect r^2 to be the same for source depth and density offset because these two quantities are not simply related by a scalar; instead, we scale D_s by a variable N^2 to obtain $\Delta\rho$ (because $\Delta\rho = -\frac{\rho_0}{g} N^2 D_s$). The higher r^2 is an artifact of this transformation, and should not be interpreted as the density offset scaling relation being superior to the source depth scaling. The mean average error and standard deviation for $\Delta\rho$ is 0.055±0.057 kgm^{-3}, while $\Delta\rho$ ranges from 0.07 to 2 kgm^{-3}. So again, Eq. (6) seems appropriate for order-of-magnitude scaling purposes.

4.3 More realistic N^2 profiles

So far, we have presented results from simulations initialized with a uniform vertical density gradient. Typically in the ocean, N^2 is small and uniform in the surface mixed layer, reaches a peak at the base of the mixed layer, and then decays below that to become small in the interior. This raises the question of whether the scaling relations hold for more realistic N^2 profile shapes. How much does the shape of the initial N^2 profile matter? In the case of non-uniform stratification, what value of N^2 should one use in Eq. (5)? To investigate this, we run three additional simulations whose initial N^2 profiles are more realistic (Fig. 9). We experiment with varying the peak N^2 value and the mixed layer depth, but we maintain the same the average stratification in the upper 250 m at 10^{-4} s^{-2} (Fig. 9). This way, the depth-integrated N^2 in the upper 250 m–which is just the density difference between the surface and 250 m–is the same. This allows us to compare the effects of only varying the shape of the density profiles, while holding the total stratification constant. In addition, the depth-averaged stratification over the full

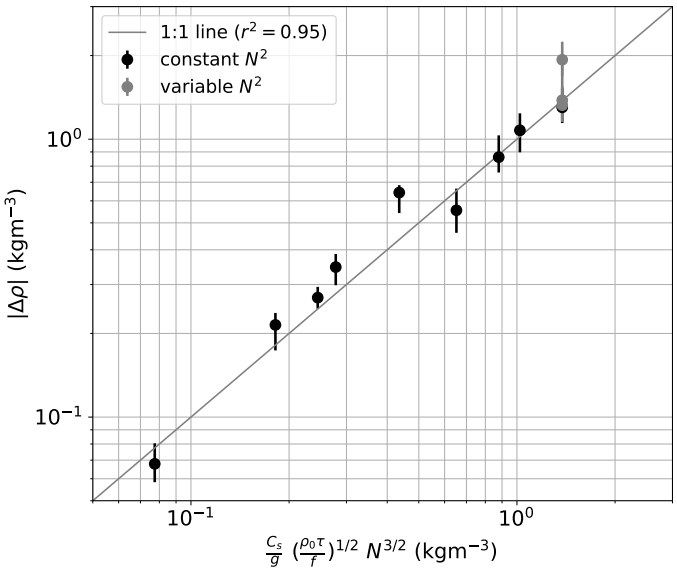

Figure 8. Density offset expressed as the difference in density between the surface and the upwelled water $\Delta\rho$ calculated from the numerical model compared to the scaling relation in Eq. (6) $\frac{C_s}{g}(\frac{\rho_0\tau}{f})^{1/2}\ N^{3/2}$. The median value is shown with error bars denoting the 10th and 90th percentiles, and the gray line shows the 1:1 line. ρ_0 is taken to be constant reference density of 1027 kg/m^3.

500 m depth is about 5.5×10^{-5} s^{-2} for the three simulations, which is the same as the medium stratification experiments (Table 3.1). A constant wind forcing of $\tau = 0.1$ Nm^{-2} is used for all three simulations, so these results are meant to be compared to the highW_highN and highW_medN experiments (Table 3.1).

The source depth and density contours for a snapshot in each of the three simulations are shown in Fig. 10. There is not a drastic difference in source depth between the small peak and deep ML experiments in Fig. 10 and Fig. 6f and i, which has the same wind stress and average stratification. However, the large peak simulation has a noticeably deeper source depth. Testing the tracer-calculated source depths against Eq. (5) with $N^2 = 10^{-4}$ s^{-2} and $N^2 = 5.5\times10^{-5}$ s^{-2} shows that a better agreement is achieved for the small peak and deep ML experiments when the higher stratification value is used. This hints that it is the total stratification in the upper ocean above the source depth that should be used in the scaling relation, and not the full water-column integrated stratification. After all, it is the upper ocean stratification that is relevant for the generation of available potential energy through upwelling and subsequent baroclinic instabilities.

The gray dots in Fig. 7 show the range of source depths from these three experiments and the scaling-predicted value using the average initial stratification in the upper 250 m. The small peak and deep ML source depths are clustered very closely around the point corresponding to the highW_highN experiment. The median source depths of the small peak, deep ML, and highW_highN simulations are 126.51 m, 131.82 m, and 124.25 m respectively, which are all within the range of the error bars. The large peak simulation has a deeper D_s of 184.36 m, although its error bars slightly overlaps with the other simulations (Fig. 7). Similarly, the density offsets of the small peak and deep ML experiments are close to that of the highW_highN simulation (Fig. 8 gray dots), while the large peak experiment has a higher density offset value.

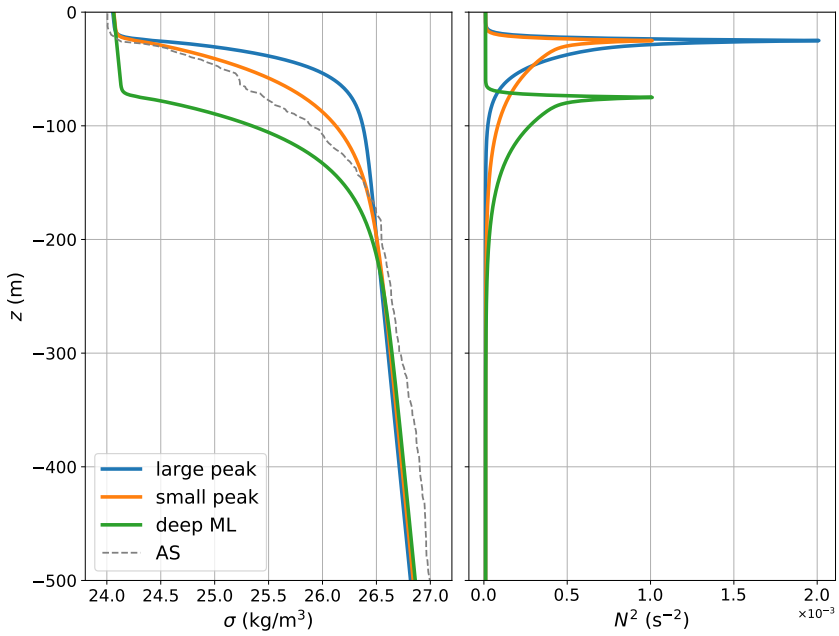

Figure 9. Initial potential density profiles minus 1000 kgm^{-3} (σ, left) and corresponding N^2 profiles (right) for the three experiments that have a non-constant initial stratification (see Table 3.1). An Argo density profile from the Arabian Sea in July 2017 is also plotted in the gray dashed line to serve as an example of a realistic density profile.

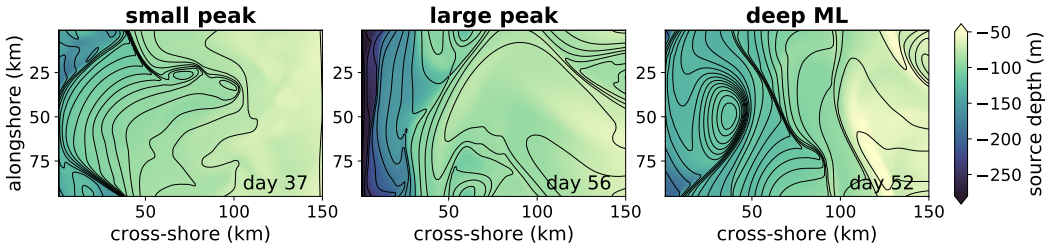

Figure 10. Same as Fig. 6 except the three simulations shown have non-uniform initial stratification profiles (see Tab. 3.1).

To understand why the large peak experiment has a deeper source depth, we can look at the nearshore density structure of these three simulations during the analysis period (Fig. 11). Despite being initialized with the same depth-integrated stratification, the nearshore stratification after the spin-up phase is actually weakest in the large peak experiment. This is because the strong initial stratification in the large peak experiment is quickly erased by the wind-driven mixing in the model, and the large peak case has the weakest initial stratification below the mixed layer (Fig. 9). Thus, the stratification that was actually present to energize the baroclinic eddies is weaker than in simulations with higher stratification below the wind-driven mixed layer. In this contrived experiment where depth-integrated N^2 was held constant, altering the mixed layer depth did not affect the source depth, but changing the N^2 peak did significantly affect D_s. The effects of the initial vertical density structure is an interesting question to investigate further in future studies.

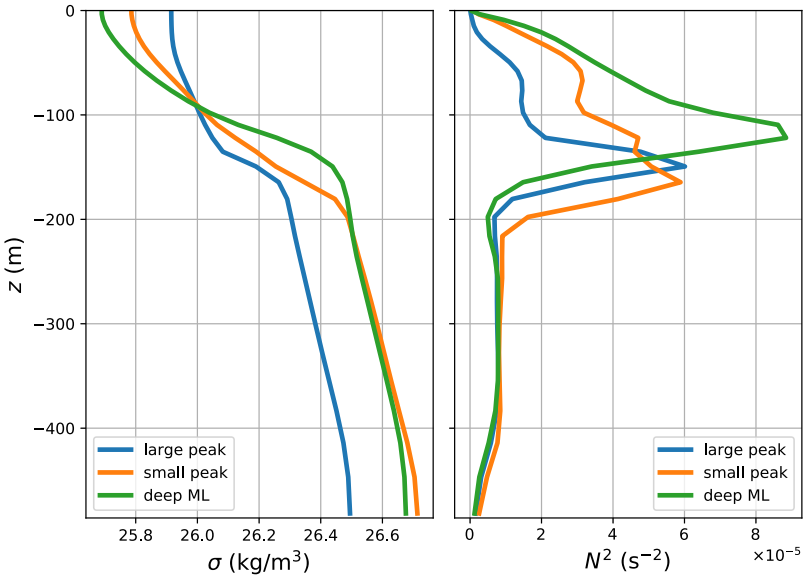

Figure 11. Nearshore density profiles minus 1000 kgm^{-3} (σ, left) and corresponding N^2 profiles (right) during period analyzed for source depth from the three experiments that have a non-constant initial stratification (see Table 3.1). Profiles for each simulation are taken on the days indicated in Fig. 10 at the location x=48 km and y=20 km.

5 Discussion

After proposing a general scaling relation for the source depth of upwelled water and verifying it with numerical experiments, we can revisit the original motivating case of the Arabian Sea and Bay of Bengal as an example of how Eq. (5) may be useful in understanding what drives the different upwelling responses. The climatological southwesterly wind stress for July in Fig. 1b-c is $\tau = 0.20$ Nm^{-2} in the AS and $\tau = 0.07$ Nm^{-2} in the BoB. The depth-averaged climatological N^2 in the upper 250 m is 1.1×10^{-4} s^{-2} and 2.1×10^{-4} s^{-2} in the western AS and BoB, respectively. Taking f for the latitude 15°N and $\rho_0 = 1027$ kg m^{-3}, Eq. 5 yields $D_s = 181$ m in the AS and $D_s = 91$ m in the BoB. Converting source depth to the density offset yields $\Delta\rho = 2.1$ kgm^{-3} in the AS and $\Delta\rho = 2.0$ kgm^{-3} for the BoB. Unsurprisingly, the source depth in the BoB is considerably shallower than the AS, which is consistent with the colder SST in the AS compared to BoB (Fig. 1). However, SST is not reflective of the similar density offset in both basins because the density in the BoB is primarily salinity driven due to large freshwater inputs from rivers and precipitation (Mahadevan et al., 2016). But beyond that, Eq. (5) allows us to quantify the relative importance of the different wind forcing and stratification on the difference in D_s between the AS and BoB. For instance, using Eq. (5) we can estimate that if the AS wind stress were reduced to a third of its value, to be equal to the BoB wind stress, it would translate into a 41% reduction in source depth. If instead the AS stratification was doubled to match the BoB (but the AS maintained its original wind stress), it would result in a 15% reduction in source depth. The difference in wind stress plays a larger role in explaining the difference in upwelling D_s between the AS and BoB, but the stratification also plays a significant role.

Furthermore, a potential implication of a shallower source depth in the BoB is a positive feedback cycle involving the Southwest Monsoon. Shallow D_s means higher SST, which leads to more convection and precipitation over the Bay of Bengal (Izumo et al., 2008). The increased precipitation further enhances stratification (or at least counter-

acts the decrease in N^2 due to upwelling) in the BoB by providing a layer of buoyant freshwater at the surface. Lastly, the persistent strong stratification contributes to a shallow upwelling source depth. McGowan et al. (2003) suggested a similar positive feedback in the California Current System where ocean warming leads to increased stratification and suppressed upwelling or shallower source depth, which further maintains high stratification. This is currently speculative, but it is interesting to note that in Fig. 1c, N^2 decreases by 0.3×10^{-4} s^{-2} from May to August in the AS as a result of strong coastal upwelling, but in the BoB N^2 only decreases by 0.1×10^{-4} s^{-2} in the same time period. The maintenance of the strong stratification in the BoB might be an example of this stratification-source depth feedback at play.

While this work is originally motivated by observations of the Arabian Sea and Bay of Bengal, the theory developed here is general and can be applied to study other coastal upwelling regions such as the EBUS, and assess how they might change with global warming. For instance, multiple studies support the Bakun hypothesis (Bakun, 1990) that alongshore winds will intensify under future warming scenarios, implying that coastal upwelling will intensify and result in increased productivity and cooler regional SSTs (Bakun, 1990; Sydeman et al., 2014; Wang et al., 2015; deCastro et al., 2016). However, many of these effects would be countered or partially mitigated by strong increases in stratification as a result of a warming oceans. This countering effect of stratification is mentioned in the literature (deCastro et al., 2016; Lorenzo et al., 2005; Auad et al., 2006), but untangling the interplay between wind, stratification, and source depth has been an open question to date (Bakun et al., 2015). Our work provides a way to quantitatively compare the relative effects of changing winds and changing stratification on upwelling source depth.

Additionally, this study has implications for the biological productivity of coastal upwelling regions. Observational and modeling studies have shown that intensifying upwelling-favorable winds do not necessarily correlate with increased primary productivity (e.g. Roemmich & McGowan, 1995; Renault et al., 2016), which highlights the necessity of considering other factors that affect nutrient supply and productivity. For example, in the well-studied California Current System, long term warming and increased stratification trends have been observed and linked to a shallower source depth (McGowan et al., 2003; Bograd & Lynn, 2003), diminished vertical fluxes of nutrients to the upper ocean (Lorenzo et al., 2005; Palacios et al., 2004), and significant ecosystem changes (McGowan et al., 2003). Our theory is consistent with these findings, and our contribution is to quantify and demonstrate a mechanism by which stratification alters the source depth. In particular, since nitrate is known to be correlated with temperature or density (e.g. Omand & Mahadevan, 2013; Palacios et al., 2013), the density offset given by Eq. (6) could be a useful metric for studying nutrient upwelling, provided that a density-nitrate relationship is known. However to fully assess biological impacts, it is important to also consider other factors. For example, reduced upwelling may be compensated by enhanced nutrients at depth (Rykaczewski & Dunne, 2010; Xiu et al., 2018), and plankton biomass may not necessarily respond to nutrient changes if there are other controls such as ecosystem food web dynamics (Xiu et al., 2018).

It is important to remember that our scaling relations, Eqs. (5) and (6), are tested using idealized numerical experiments which neglect several factors. To begin, we force the model with a constant wind that blows for months, but in reality the wind is intermittent and varies on a time scale of days with strong bursts and weak periods. Our scaling does not account for variable τ in time or space, but is meant to represent the effects of the average alongshore wind stress over the course of an upwelling season. This work does not describe the increase in source depth over the course of days, such as when upwelling-favorable winds commence at the beginning of the upwelling season. Equations. (5) and (6) instead are meant to estimate D_s and $\Delta\rho$ over multiple weeks during the upwelling season, where we can assume an approximate balance of the mean ψ_w and ψ_e in that time span. Additionally, this work is focused on the near-shore region where Ek-

man transport dominates, and we do not consider the effect of Ekman pumping due to a wind stress curl, though Jacox and Edwards (2012) found that the shape of the cross-shore wind profile did have an effect on the upwelling source depth. Capet et al. (2004) also showed that different cross-shore wind profiles impacted the patterns of upwelling circulation, surface temperature, and biogeochemistry off the Californian coast. Furthermore, we present a source depth scaling based on local forcing, but source depth can also be affected by large scale climate variability modes such as the El Niño-Southern Oscillation (Jacox et al., 2015), Pacific Decadal Oscillation (Chhak & Lorenzo, 2007) and the North Pacific Gyre Oscillation (Di Lorenzo et al., 2008).

Lastly, the sloping topography, which is not addressed here, would result in some onshore transport along the bottom boundary layer (Lentz & Chapman, 2004; Jacox & Edwards, 2011, 2012) and also alter the eddy dynamics (Brink, 2016). The inclusion of topography would require re-working the scaling relation to include bottom stress as another mechanism for balancing the wind, and this is beyond the scope of this study.

6 Conclusion

We investigate the role of stratification and alongshore wind stress on the source depth in a coastal upwelling region. To our knowledge, there has been no study to date on the source depth in coastal upwelling regions that considers the role of submesoscale eddies. We present a scaling relation for the source depth at dynamic equilibrium that depends on a balance between the wind-driven Ekman circulation and the eddy restratifying overturning circulation which shows that the source depth $D_s = C_s(\frac{\tau}{\rho_0 N f})^{1/2}$. This can be converted to a density offset scaling by considering the change in density from the surface to the source depth: $\Delta\rho = \frac{C_s}{g}(\frac{\rho_0 \tau}{f})^{1/2} N^{3/2}$. The result of increasing source depth with weaker stratification is qualitatively consistent with previous studies (Jacox & Edwards, 2011, 2012; Oerder et al., 2015), but now we are able to quantify the effects of wind stress and stratification on the source depth. A main takeaway from our study is that both the source depth and the density offset depends nonlinearly on the stratification N and wind stress, and they contribute equally to the source depth. Thus, as stratification increases more drastically in a warming planet, the stratification will play a more important role in decreasing the source depth. That may have implications for increasing SST, which has a positive feedback, and in changing nutrient supply for primary production, which are areas of future study.

Acknowledgments

We thank Kenneth H. Brink for discussions and for providing feedback an early version of this manuscript. This work was funded by the ONR grant N000014-17-1-2390, and JH was supported by the NASA FINESST grant 80NSSC19K1350).

Datasets for Fig. 1 are described in Dee et al. (2011) and Schmidtko et al. (2013), and they are accessible here https://www.ecmwf.int/en/forecasts/datasets/reanalysis-datasets/era-interim, https://www.pmel.noaa.gov/mimoc/. Source code to reproduce the model runs can be found at http://doi.org/10.5281/zenodo.4757609.

References

Allen, J. S., Newberger, P. A., & Federiuk, J. (1995). Upwelling circulation on the Oregon continental shelf. Part I: Response to idealized forcing. *Journal of Physical Oceanography*, *25*(8), 1843–1866. doi: https://doi.org/10.1175/1520-0485(1995)025⟨1843:UCOTOC⟩2.0.CO;2

Andrews, D. G., & McIntyre, M. E. (1976). Planetary waves in horizontal and vertical shear: The generalized Eliassen-Palm relation and the mean zonal

acceleration. *Journal of the Atmospheric Sciences*, *33*(11), 2031–2048. doi: https://doi.org/10.1175/1520-0469(1976)033⟨2031:pwihav⟩2.0.co;2

Auad, G., Miller, A., & Di Lorenzo, E. (2006). Long-term forecast of oceanic conditions off California and their biological implications. *Journal of Geophysical Research: Oceans*, *111*(C9). doi: https://doi.org/10.1029/2005JC003219

Bakun, A. (1990). Global climate change and intensification of coastal ocean upwelling. *Science*, *247*(4939), 198–201. doi: https://doi.org/10.1126/science.247.4939.198

Bakun, A., Black, B., Bograd, S., García-Reyes, M., Miller, A., Rykaczewki, R., & Sydeman, W. (2015). Anticipated effects of climate change on coastal upwelling ecosystems. *Current Climate Change Reports*, *1*, 85–93. doi: https://doi.org/10.1007/s40641-015-0008-4

Bograd, S. J., & Lynn, R. J. (2003). Long-term variability in the Southern California Current System. *Deep Sea Research Part II: Topical Studies in Oceanography*, *50*(14), 2355–2370. doi: https://doi.org/10.1016/S0967-0645(03)00131-0

Brink, K. (1983). The near-surface dynamics of coastal upwelling. *Progress in Oceanography*, *12*(3), 223-257. doi: https://doi.org/10.1016/0079-6611(83)90009-5

Brink, K. (2016). Continental shelf baroclinic instability. Part I: Relaxation from upwelling or downwelling. *Journal of Physical Oceanography*, *46*(2), 551–568. doi: https://doi.org/10.1175/JPO-D-15-0047.1

Brink, K., & Seo, H. (2016). Continental shelf baroclinic instability. Part II: Oscillating wind forcing. *Journal of Physical Oceanography*, *46*(2), 569 –582. doi: https://doi.org/10.1175/JPO-D-15-0048.1

Capet, X. J., Marchesiello, P., & McWilliams, J. C. (2004). Upwelling response to coastal wind profiles. *Geophysical Research Letters*, *31*(13). doi: https://doi.org/10.1029/2004GL020123

Capet, X. J., McWilliams, J. C., Molemaker, M. J., & Shchepetkin, A. F. (2008). Mesoscale to submesoscale transition in the California Current System. Part II: Frontal processes. *Journal of Physical Oceanography*, *38*(1), 44 – 64. doi: https://doi.org/10.1175/2007JPO3672.1

Carmack, E. C., & Aagaard, K. (1977). A note on volumetric considerations of upwelling in the Benguela Current. *Estuarine and Coastal Marine Science*, *5*(1), 135–142. doi: https://doi.org/10.1016/0302-3524(77)90078-0

Carr, M.-E. (2001). Estimation of potential productivity in Eastern Boundary Currents using remote sensing. *Deep Sea Research Part II: Topical Studies in Oceanography*, *49*(1), 59–80. doi: https://doi.org/10.1016/S0967-0645(01)00094-7

Carr, M.-E., & Kearns, E. J. (2003). Production regimes in four Eastern Boundary Current systems. *Deep Sea Research Part II: Topical Studies in Oceanography*, *50*(22), 3199–3221. doi: https://doi.org/10.1016/j.dsr2.2003.07.015

Cerovečki, I., Plumb, R. A., & Heres, W. (2009). Eddy Transport and Mixing in a Wind- and Buoyancy-Driven Jet on the Sphere. *Journal of Physical Oceanography*, *39*(5), 1133–1149. doi: https://doi.org/10.1175/2008JPO3596.1

Cessi, P. (1996). Gridscale instability of convective-adjustment schemes. *Journal of Marne Research*, *54*(3), 407–420. doi: https://doi.org/10.1357/0022240963213529

Chavez, F. P., & Messié, M. (2009). A comparison of Eastern Boundary Upwelling Ecosystems. *Progress in Oceanography*, *83*(1-4), 80–96. doi: https://doi.org/10.1016/j.pocean.2009.07.032

Chhak, K., & Lorenzo, E. D. (2007). Decadal variations in the California Current upwelling cells. *Geophysical Research Letters*, *34*(14). doi: https://doi.org/10.1029/2007GL030203

deCastro, M., Sousa, M. C., Santos, F., Dias, J. M., & Gómez-Gesteira, M. (2016). How will Somali coastal upwelling evolve under future warming scenarios?

Scientific Reports, *6*(1). Retrieved from `http://www.nature.com/articles/srep30137` doi: https://doi.org/10.1038/srep30137

Dee, D. P., Uppala, S. M., Simmons, A. J., Berrisford, P., Poli, P., Kobayashi, S., & et al. (2011). The ERA-Interim reanalysis: configuration and performance of the data assimilation system. *Quarterly Journal of the Royal Meteorological Society*, *137*(656), 553–597. doi: https://doi.org/10.1002/qj.828

Dever, E., Dorman, C., & Largier, J. (2006). Surface boundary-layer variability off Northern California, USA, during upwelling. *Deep Sea Research Part II: Topical Studies in Oceanography*, *53*(25), 2887–2905. doi: https://doi.org/10.1016/j.dsr2.2006.09.001

Di Lorenzo, E., Schneider, N., Cobb, K. M., Franks, P. J. S., Chhak, K., Miller, A. J., & et al. (2008). North Pacific Gyre Oscillation links ocean climate and ecosystem change. *Geophysical Research Letters*, *35*(8). doi: https://doi.org/10.1029/2007GL032838

Durski, S. M., & Allen, J. (2005). Finite-amplitude evolution of instabilities associated with the coastal upwelling front. *Journal of physical oceanography*, *35*(9), 1606–1628. doi: https://doi.org/10.1175/JPO2762.1

Enriquez, A. G., & Friehe, C. A. (1995). Effects of wind stress and wind stress curl variability on coastal upwelling. *Journal of Physical Oceanography*, *25*(7), 1651–1671. doi: https://doi.org/10.1175/1520-0485(1995)025⟨1651:EOWSAW⟩2.0.CO;2

Fox-Kemper, B., & Ferrari, R. (2008b). Parameterization of mixed layer eddies. Part II: Prognosis and impact. *Journal of Physical Oceanography*, *38*(6), 1166–1179. doi: https://doi.org/10.1175/2007JPO3788.1

Fox-Kemper, B., Ferrari, R., & Hallberg, R. (2008a). Parameterization of mixed layer eddies. Part I: Theory and diagnosis. *Journal of Physical Oceanography*, *38*(6), 1145–1165. doi: https://doi.org/10.1175/2007JPO3792.1

Friederich, G. E., Ledesma, J., Ulloa, O., & Chavez, F. P. (2008). Air–sea carbon dioxide fluxes in the coastal southeastern tropical Pacific. *Progress in Oceanography*, *79*(2), 156–166. doi: https://doi.org/10.1016/j.pocean.2008.10.001

Gruber, N., Lachkar, Z., Frenzel, H., Marchesiello, P., Münnich, M., McWilliams, J. C., & et al. (2011). Eddy-induced reduction of biological production in eastern boundary upwelling systems. *Nature Geoscience*, *4*(11), 787–792. doi: https://doi.org/10.1038/ngeo1273

Hales, B., Takahashi, T., & Bandstra, L. (2005). Atmospheric CO2 uptake by a coastal upwelling system. *Global Biogeochemical Cycles*, *19*(1). doi: https://doi.org/10.1029/2004GB002295

Held, I. M., & Schneider, T. (1999). The surface branch of the zonally averaged mass transport circulation in the troposphere. *Journal of the Atmospheric Sciences*, *56*(11), 1688–1697. doi: https://doi.org/10.1175/1520-0469(1999)056⟨1688:TSBOTZ⟩2.0.CO;2

Hernández-Carrasco, I., Rossi, V., Hernández-García, E., Garçon, V., & López, C. (2014). The reduction of plankton biomass induced by mesoscale stirring: A modeling study in the Benguela upwelling. *Deep Sea Research Part I: Oceanographic Research Papers*, *83*, 65–80. doi: https://doi.org/10.1016/j.dsr.2013.09.003

Huyer, A. (1983). Coastal upwelling in the California current system. *Progress in Oceanography*, *12*(3), 259–284. doi: https://doi.org/10.1016/0079-6611(83)90010-1

Izumo, T., Montégut, C. B., Luo, J.-J., Behera, S. K., Masson, S., & Yamagata, T. (2008). The role of the western Arabian Sea upwelling in Indian monsoon rainfall variability. *Journal of Climate*, *21*(21), 5603–5623. doi: https://doi.org/10.1175/2008JCLI2158.1

Jacox, M. G., & Edwards, C. A. (2011). Effects of stratification and shelf slope on nutrient supply in coastal upwelling regions. *Journal of Geophysical Research*,

116(C3). doi: https://doi.org/10.1029/2010JC006547

Jacox, M. G., & Edwards, C. A. (2012). Upwelling source depth in the presence of nearshore wind stress curl. *Journal of Geophysical Research: Oceans*, *117*(C5). doi: https://doi.org/10.1029/2011JC007856

Jacox, M. G., Fiechter, J., Moore, A. M., & Edwards, C. A. (2015). ENSO and the California Current coastal upwelling response. *Journal of Geophysical Research: Oceans*, *120*(3), 1691–1702. doi: https://doi.org/10.1002/2014JC010650

Koračin, D., Dorman, C. E., & Dever, E. P. (2004). Coastal perturbations of marine-layer winds, wind stress, and wind stress curl along California and Baja California in June 1999. *Journal of Physical Oceanography*, *34*(5), 1152–1173. doi: https://doi.org/10.1175/1520-0485(2004)034⟨1152:cpomww⟩2.0.co;2

Large, W. G., & Pond, S. (1981). Open ocean momentum flux measurements in moderate to strong winds. *Journal of Physical Oceanography*, *11*(3), 324–336. doi: https://doi.org/10.1175/1520-0485(1981)011⟨0324:oomfmi⟩2.0.co;2

Lee, M.-M., Marshall, D. P., & Williams, R. G. (1997). On the eddy transfer of tracers: Advective or diffusive? *Journal of Marine Research*, *55*(3), 483–505. doi: https://doi.org/10.1357/0022240973224346

Lentz, S. J. (1992). The surface boundary layer in coastal upwelling regions. *Journal of Physical Oceanography*, *22*(12), 1517–1539. doi: https://doi.org/10.1175/1520-0485(1992)022⟨1517:TSBLIC⟩2.0.CO;2

Lentz, S. J., & Chapman, D. C. (2004). The importance of nonlinear cross-shelf momentum flux during wind-driven coastal upwelling. *Journal of Physical Oceanography*, *34*(11), 2444–2457. doi: https://doi.org/10.1175/JPO2644.1

Lorenzo, E. D., Miller, A. J., Schneider, N., & McWilliams, J. C. (2005). The warming of the California Current System: Dynamics and ecosystem implications. *Journal of Physical Oceanography*, *35*(3), 336 – 362. doi: https://doi.org/10.1175/JPO-2690.1

Mahadevan, A., Jaeger, G. S., Freilich, M., Omand, M. M., Shroyer, E. L., & Sengupta, D. (2016). Freshwater in the bay of bengal: Its fate and role in air-sea heat exchange. *Oceanography*, *29*(2), 72–81. doi: https://doi.org/10.5670/oceanog.2016.40

Mahadevan, A., Oliger, J., & Street, R. (1996a). A nonhydrostatic mesoscale ocean model. Part I: Well-posedness and scaling. *Journal of Physical Oceanography*, *26*(9), 1868–1880. doi: https://doi.org/10.1175/1520-0485(1996)026⟨1868:anmomp⟩2.0.co;2

Mahadevan, A., Oliger, J., & Street, R. (1996b). A nonhydrostatic mesoscale ocean model. Part II: Numerical implementation. *Journal of Physical Oceanography*, *26*(9), 1881–1900. doi: https://doi.org/10.1175/1520-0485(1996)026⟨1881:anmomp⟩2.0.co;2

Mahadevan, A., Tandon, A., & Ferrari, R. (2010). Rapid changes in mixed layer stratification driven by submesoscale instabilities and winds. *Journal of Geophysical Research: Oceans*, *115*(C3). doi: https://doi.org/10.1029/2008JC005203

Marshall, J., & Radko, T. (2003). Residual-mean solutions for the Antarctic Circumpolar Current and its associated overturning circulation. *Journal of Physical Oceanography*, *33*(11), 2341–2354. doi: https://doi.org/10.1175/1520-0485(2003)033⟨2341:RSFTAC⟩2.0.CO;2

McDougall, T., & Barker, P. (2011, 01). Getting started with TEOS-10 and the Gibbs Seawater (GSW) Oceanographic Toolbox. *SCOR/IAPSO WG*, *127*, 1–28.

McGowan, J. A., Bograd, S. J., Lynn, R. J., & Miller, A. J. (2003). The biological response to the 1977 regime shift in the California Current. *Deep Sea Research Part II: Topical Studies in Oceanography*, *50*(14), 2567–2582. doi: https://doi.org/10.1016/S0967-0645(03)00135-8

Messié, M., Ledesma, J., Kolber, D. D., Michisaki, R. P., Foley, D. G., & Chavez, F. P. (2009). Potential new production estimates in four eastern boundary upwelling ecosystems. *Progress in Oceanography*, *83*(1), 151–158. doi: https://doi.org/10.1016/j.pocean.2009.07.018

Mukherjee, S., Ramachandran, S., Tandon, A., & Mahadevan, A. (2016). Production and destruction of eddy kinetic energy in forced submesoscale eddy-resolving simulations. *Ocean Modelling*, *105*, 44-59.

Oerder, V., Colas, F., Echevin, V., Codron, F., Tam, J., & Belmadani, A. (2015). Peru-Chile upwelling dynamics under climate change. *Journal of Geophysical Research: Oceans*, *120*(2), 1152–1172. doi: https://doi.org/10.1002/2014jc010299

Omand, M. M., & Mahadevan, A. (2013). Large-scale alignment of oceanic nitrate and density. *Journal of Geophysical Research: Oceans*, *118*(10), 5322–5332. doi: https://doi.org/10.1002/jgrc.20379

Palacios, D. M., Bograd, S. J., Mendelssohn, R., & Schwing, F. B. (2004). Long-term and seasonal trends in stratification in the California Current, 1950–1993. *Journal of Geophysical Research: Oceans*, *109*(C10). doi: https://doi.org/10.1029/2004JC002380

Palacios, D. M., Hazen, E. L., Schroeder, I. D., & Bograd, S. J. (2013). Modeling the temperature-nitrate relationship in the coastal upwelling domain of the California Current. *Journal of Geophysical Research: Oceans*, *118*(7), 3223–3239. doi: https://doi.org/10.1002/jgrc.20216

Pickett, M. H., & Paduan, J. D. (2003). Ekman transport and pumping in the California Current based on the U.S. Navy's high-resolution atmospheric model (COAMPS). *Journal of Geophysical Research: Oceans*, *108*(C10). doi: https://doi.org/10.1029/2003JC001902

Pollard, R. T., Rhines, P. B., & Thompson, R. O. R. Y. (1973). The deepening of the wind-Mixed layer. *Geophysical Fluid Dynamics*, *4*(4), 381–404. doi: https://doi.org/10.1080/03091927208236105

Prasanna Kumar, S., Muraleedharan, P. M., Prasad, T. G., Gauns, M., Ramaiah, N., Souza, S. N. d., ... Madhupratap, M. (2002). Why is the Bay of Bengal less productive during summer monsoon compared to the Arabian Sea? *Geophysical Research Letters*, *29*(24), 88–1–88–4. Retrieved from `https://doi.org/10.1029/2002gl016013` doi: 10.1029/2002GL016013

Renault, L., Deutsch, C., McWilliams, J. C., Frenzel, H., Liang, J.-H., & Colas, F. (2016). Partial decoupling of primary productivity from upwelling in the California Current system. *Nature Geoscience*, *9*(7), 505–508. doi: https://doi.org/10.1038/ngeo2722

Roemmich, D., & McGowan, J. (1995). Climatic warming and the decline of zooplankton in the California Current. *Science*, *267*(5202), 1324–1326. doi: https://doi.org/10.1126/science.267.5202.1324

Rykaczewski, R. R., & Dunne, J. P. (2010). Enhanced nutrient supply to the California Current Ecosystem with global warming and increased stratification in an earth system model. *Geophysical Research Letters*, *37*(21). doi: https://doi.org/10.1029/2010GL045019

Schmidtko, S., Johnson, G. C., & Lyman, J. M. (2013). MIMOC: A global monthly isopycnal upper-ocean climatology with mixed layers. *Journal of Geophysical Research: Oceans*, *118*(4), 1658–1672. doi: https://doi.org/10.1002/jgrc.20122

Sydeman, W. J., García-Reyes, M., Schoeman, D. S., Rykaczewski, R. R., Thompson, S. A., Black, B. A., & Bograd, S. J. (2014). Climate change and wind intensification in coastal upwelling ecosystems. *Science*, *345*(6192), 77–80. doi: https://doi.org/10.1126/science.1251635

Szoeke, R. A. D., & Richman, J. G. (1984). On wind-driven mixed layers with strong horizontal gradients—a theory with application to coastal upwelling.

Journal of Physical Oceanography, *14*(2), 364 –377. doi: https:/doi.org/10.1175/1520-0485(1984)014⟨0364:OWDMLW⟩2.0.CO;2

Torres, R., Turner, D., Rutllant, J., Sobarzo, M., Antezana, T., & Gonzalez, H. E. (2002). CO_2 outgassing off central Chile (31–30°S) and northern Chile (24–23°S) during austral summer 1997: the effect of wind intensity on the upwelling and ventilation of CO_2-rich waters. *Deep Sea Research Part I: Oceanographic Research Papers*, *49*(8), 1413–1429. doi: https://doi.org/10.1016/S0967-0637(02)00034-1

Wang, D., Gouhier, T. C., Menge, B. A., & Ganguly, A. R. (2015). Intensification and spatial homogenization of coastal upwelling under climate change. *Nature*, *518*(7539), 390–394. doi: https://doi.org/10.1038/nature14235

Wijesekera, H. W., Allen, J. S., & Newberger, P. A. (2003). Modeling study of turbulent mixing over the continental shelf: Comparison of turbulent closure schemes. *Journal of Geophysical Research: Oceans*, *108*(C3). doi: https://doi.org/10.1029/2001JC001234

Xiu, P., Chai, F., Curchitser, E., & Castruccio, F. (2018). Future changes in coastal upwelling ecosystems with global warming: The case of the California Current System. *Scientific Reports*, *8*(2866). doi: https://doi.org/10.1038/s41598-018-21247-7